Physics in Medicine & Biology

IPEM Institute of Physics and Engineering in Medicine

PAPER • OPEN ACCESS

Image-based view-angle independent cardiorespiratory motion gating and coronary sinus catheter tracking for x-ray-guided cardiac electrophysiology procedures

To cite this article: Maria Panayiotou *et al* 2015 *Phys. Med. Biol.* **60** 8087

OPEN ACCESS
IOP Publishing | Institute of Physics and Engineering in Medicine Physics in Medicine & Biology
Phys. Med. Biol. **60** (2015) 8087–8108 doi:10.1088/0031-9155/60/20/8087

Image-based view-angle independent cardiorespiratory motion gating and coronary sinus catheter tracking for x-ray-guided cardiac electrophysiology procedures

Maria Panayiotou[1], Kawal S Rhode[1], Andrew P King[1], Yingliang Ma[1], Michael Cooklin[2], Mark O'Neill[2], Jaswinder Gill[2], C A Rinaldi[2] and R James Housden[1]

[1] Division of Imaging Sciences and Biomedical Engineering, King's College London, London SE1 7EH, UK
[2] Department of Cardiology, Guy's and St. Thomas' Hospitals NHS Foundation Trust, London, UK

E-mail: maria.panayiotou@kcl.ac.uk

Received 12 June 2015, revised 3 August 2015
Accepted for publication 30 August 2015
Published 1 October 2015

Abstract

Determination of the cardiorespiratory phase of the heart has numerous applications during cardiac imaging. In this article we propose a novel view-angle independent near-real time cardiorespiratory motion gating and coronary sinus (CS) catheter tracking technique for x-ray fluoroscopy images that are used to guide cardiac electrophysiology procedures. The method is based on learning CS catheter motion using principal component analysis and then applying the derived motion model to unseen images taken at arbitrary projections, using the epipolar constraint. This method is also able to track the CS catheter throughout the x-ray images in any arbitrary subsequent view. We also demonstrate the clinical application of our model on rotational angiography sequences. We validated our technique in normal and very low dose phantom and clinical datasets. For the normal dose clinical images we established average systole, end-expiration and end-inspiration gating success rates of 100%, 85.7%, and 92.3%, respectively. For very low dose applications, the technique was able to track the CS catheter with median errors not exceeding 1 mm for all tracked electrodes. Average gating success rates of 80.3%, 71.4%,

and 69.2% were established for the application of the technique on clinical datasets, even with a dose reduction of more than 10 times. In rotational sequences at normal dose, CS tracking median errors were within 1.2 mm for all electrodes, and the gating success rate was 100%, for view angles from RAO 90° to LAO 90°. This view-angle independent technique can extract clinically useful cardiorespiratory motion information using x-ray doses significantly lower than those currently used in clinical practice.

Keywords: cardiorespiratory motion gating, principal component analysis, cardiac electrophysiology, 3D rotational angiography, x-ray fluoroscopy

(Some figures may appear in colour only in the online journal)

1. Introduction

Electrophysiology (EP) procedures are minimally invasive catheterization procedures that are used to treat cardiac arrhythmias. These procedures are typically performed using 2D x-ray fluoroscopy to guide the insertion and movement of catheters. While x-ray fluoroscopy provides high temporal and spatial resolution, the guidance of such procedures is compromised by the inability of x-ray to effectively visualise soft tissues. In order to enhance image guidance for such cardiac interventions, intra-procedure x-ray fluoroscopy images can be registered and overlaid with pre-procedural 3D anatomical models derived from other imaging modalities, such as magnetic resonance imaging (MRI) (De Buck *et al* 2005, Rhode *et al* 2005, Gutiérrez *et al* 2007) and computed tomography (CT) (Sra *et al* 2006). X-ray fluoroscopy images can also be registered and overlaid with 3D rotational x-ray angiography (3DRXA), which is particularly suited to the clinical workflow (Li *et al* 2009). However, the anatomical models will be static and will not update with the intra-procedural situation. Cardiorespiratory motion causes mis-registration of these models and this must be corrected by motion compensation techniques, which require the cardiorespiratory phase to be determined in real time.

Motion gating is useful to obtain synchronised x-ray views at two oblique angles. These can provide image registration of the pre-procedure image (Truong *et al* 2009) both for procedure guidance and for the off-line fusion of cardiac image data for applications in biophysical modelling research. Synchronised x-ray views are also important when performing catheter-based ablation treatment or electrical measurement. The treatment or measurement sites relative to an anatomical model are often determined using sequential biplane x-ray, both for procedure guidance and for retrospective biophysical modelling (Rhode and Sermesant 2011). Motion compensation via gating is crucial for achieving the required accuracy.

One technique for cardiac gating is by synchronizing the fluoroscopic images with the electrocardiogram. However, this requires extra hardware, is normally an optional extra when purchasing an x-ray system and, when present, there may be latency between the acquisition of the ECG and x-ray data that needs to be calibrated for accurate gating. Respiratory gating can be achieved using the breath-hold technique, commonly used during MRI (Paling and Brookeman 1986, Mageras and Yorke 2004), although this is not practical in the catheter laboratory where patients can be heavily sedated. Furthermore, respiratory motion can be handled by the use of external fiducial markers placed on the patient's body (Khamene *et al* 2004).

Alternatively, detecting the cardiorespiratory phase using the fluoroscopy images is more suited to the routine clinical workflow, as this does not require any fiducial markers, or special hardware. Image-based methods can be divided into those that measure respiratory phase only, cardiac phase only and both. Methods of measuring the respiratory phase only

include diaphragm (Condurache *et al* 2005, Timinger *et al* 2005, Ma *et al* 2009), heart border (Ma *et al* 2012) and EP catheter (Brost *et al* 2009, 2010, Ma *et al* 2010) tracking. Other methods for measuring the respiratory phase have studied the motion of the coronary tree using 2D biplane angiograms (Shechter *et al* 2004, Schneider *et al* 2010), or the motion of left atrial structures such as the pulmonary veins and mitral valve annulus (Ector *et al* 2008). In King *et al* (2009a) and King *et al* (2009b) an affine motion model for the heart was computed from a series of MRI volumes, and the affine parameters were fitted to polynomial functions of the diaphragm position. The model was applied by tracking the diaphragm position in the x-ray fluoroscopy imaging and updating the roadmap accordingly. Methods of measuring the cardiac phase only include weighted centroid tracking (Lehmann *et al* 2006). Measuring both types of motion simultaneously is an advantage. Successful methods include the use of phase-correlation between successive x-ray images (Sundar *et al* 2009) and model-based approaches such as the hierarchical manifold learning based (Panayiotou *et al* 2014) and the Masked-PCA based (Panayiotou *et al* 2014b) techniques. Nevertheless, because these are model-based approaches a separate model should be formed every time the angulation of the scanner is changed between frames. Moreover, they are retrospective approaches and consequently, real-time application is not possible. Additionally, a technique that relies on tracking of a circumferential mapping catheter when it is in firm contact with a pulmonary vein during ablation for atrial fibrillation (Brost *et al* 2012) has been proposed, but this is not generally applicable to other interventional procedures.

We have previously proposed a technique for automated image-based near-real time cardiorespiratory motion gating in normal and very low dose x-ray fluoroscopy images (Panayiotou *et al* 2013). The technique can determine cardiorespiratory phase and gate previously unseen frames based on a statistical model formed from normal dose images. This model is acquired from a calibration sequence using principal component analysis (PCA) of the motion of the coronary sinus (CS) catheter, a particular catheter that is nearly always present in EP procedures. One major limitation of this and other model-based approaches is the requirement to build a separate model for each x-ray view.

In addition to the above applications of motion compensation and synchronisation of sequential bi-plane images, cardio-respiratory phase determination is also important in rotational sequences for gating of rotational coronary angiography and of C-arm CT. In this application, the view-angle of the x-ray is changing continuously, such that none of the above mentioned image-based methods could be used. To the authors knowledge the only view-angle independent work in the literature is proposed by Lehmann *et al* (2006). The technique is capable of measuring coronary motion from the 2D projection images acquired during rotational angiography, with the aim of developing an image-based cardiac gating strategy specifically for 3D coronary angiography. The image-based technique is based on the weighted centroid of the opacified coronary arteries. The 1D vector component of the centroid that is parallel to the axis of rotation is chosen as the image-based metric of motion. In coronary angiography the patient's superior-inferior (SI) axis is roughly aligned with the detector's axis of rotation, therefore the image-based metric of motion is the SI component of the weighted centroid (SIC), and this is used to track vessel motion. However, the 1D vector component of the centroid that is parallel to the axis of rotation is independent of the angular position of the detector. Therefore, this technique has the advantage of being view angle independent. Nevertheless, the technique's robustness as a function of angle is not fully tested as the authors analysed data from only two views. Clinically, where small field-of-view x-ray image intensifier detectors are used in coronary angiography, the background structures may move in and out of the field of view and it is important that the effect of this on the SIC measurement be minimized. An additional drawback of this technique is that it can only gate the cardiac

motion of the heart. The utility of the technique in 3D coronary angiography has been demonstrated in an animal study. The success of the animal experiment is encouraging, but further analysis of 3D clinical angiograms is necessary.

In this paper, we significantly extend our previous approach (Panayiotou *et al* 2013) to make it x-ray system view-angle independent and therefore much more clinically useful. Our proposed approach again forms a PCA-based model of the CS catheter in a first or *training* view. It then uses this to determine both the cardiac and the respiratory phases in near-real time in any arbitrary second or *current* view. Along with cardiorespiratory motion determination, this technique is able to track the 2D CS catheter electrode positions, again in any arbitrary subsequent view. Thus it is possible to obtain synchronised electrode positions in the two views. The main scientific contributions of this paper are:

- Determination of both the cardiac and the respiratory phases in near-real time in any arbitrary view without retraining;
- 2D tracking of the CS catheter in any arbitrary view, including those in which other electrode detection methods fail.

We carry out comprehensive validation of our gating and CS tracking technique on clinical and phantom x-ray sequences. In particular, we show how this novel approach can be used for motion gating of 3DRXA for which current methods are limited to breath-holding for respiration and either no gating for cardiac motion or arresting the heart using adenosine or rapid pacing (Kriatselis *et al* 2011).

2. Methods

In this section we first describe the formation of our statistical model of catheter motion in the training view (section 2.1), explicitly described in our previous work (Panayiotou *et al* 2013), and then its application on the current view (section 2.2), which is the novel contribution of this work. Figure 1 gives an overview of our proposed workflow.

2.1. Statistical model formation in the training view

The formation of our statistical model comprises two main steps. Firstly, the technique described in Ma *et al* (2010) is used to track the electrodes of the CS catheter throughout the x-ray sequence. Secondly, PCA is applied to the coordinates of the tracked electrodes. The reasons for choosing the CS catheter instead of other catheters are that it is routinely used during EP procedures, it remains in place throughout the procedure, its position is usually not altered and it is rarely overlapped by other catheters in the x-ray projections. This is due to the positioning of the main part of the CS along the border of the mitral valve annulus. Additionally, since the main part of the CS is a curved structure, it has similar foreshortening in all routinely used x-ray projections, which makes it an ideal choice for derivation of motion. The steps are described below.

2.1.1. CS catheter detection. The CS catheter used here is composed of 10 electrodes, distributed in pairs along the catheter. The CS tracking technique (Ma *et al* 2010) uses a fast multi-scale blob detection method (Lindeberg 1993) to detect all electrode-like objects in an x-ray image and a cost function to discriminate the CS catheter from other catheters. After application of the tracking algorithm for all frames in the training view, θ_1, the x and y positions of each of the 10 electrodes are concatenated into a single column vector for each time point. Hence, the data generated by the tracking process consists of:

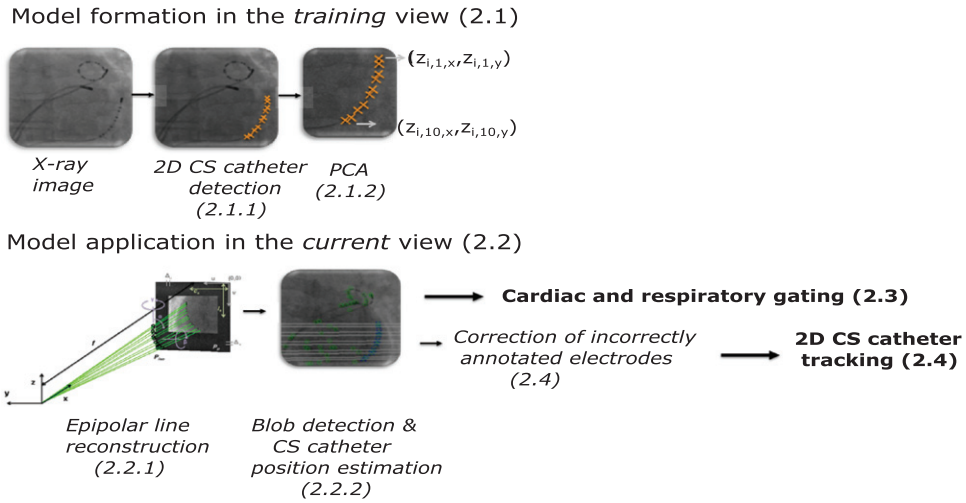

Figure 1. Illustration of proposed workflow. The section numbers (2.1, 2.2, etc) refer to the corresponding section numbers in the text, and the bold text indicates the two outputs of the algorithm.

$$\mathbf{s}_i = (z_{i,1,x}, z_{i,1,y}, \ldots, z_{i,10,x}, z_{i,10,y})^T, 1 \leqslant i \leqslant N \tag{1}$$

where $z_{i,e,x}$ and $z_{i,e,y}$ represent the x and y coordinates of the eth electrode in the ith frame. $e = 1$ corresponds to the distal electrode, and N is the number of frames.

2.1.2. Principal component analysis. PCA transforms a multivariate dataset of possibly correlated variables into a new dataset of a smaller number of uncorrelated variables called principal components (PCs), without any loss of information (Jolliffe 2002). We first compute the mean vector, $\bar{\mathbf{s}}$, and the covariance matrix, $\mathbf{S}$. The eigenvectors $\mathbf{v}_m, 1 \leqslant m \leqslant M$ of $\mathbf{S}$ represent the PCs and the corresponding eigenvalues $d_m, 1 \leqslant m \leqslant M$ represent the variance of the data along the direction of the eigenvectors. For our application $M = 20$ since the $\mathbf{s}_i$ are of length 20. The result of the PCA gives possible CS catheter electrode positions in θ_1. It was found, by correlation with our gold standard cardiorespiratory motion, that the first and second modes of variation represented the cardiac and respiratory motions, respectively (Panayiotou *et al* 2013).

2.2. Application of statistical model on the current view

The task is to gate previously unseen frames in near-real time in any arbitrary second or current view based on a statistical model formed in a first or training view. The gating is prospective in the sense that we do not need to collect the whole sequence before processing, although it will be performed with a time lag of 1 sample interval because of the need to identify peaks/troughs in the extracted signals. Consequently, the gating is almost prospective, but because of the phase lag it will be called 'near real-time gating'.

2.2.1. Epipolar line reconstruction. Epipolar reconstruction allows loss of depth information to be recovered from a 2D projection image if another 2D image is taken of the same target from a different view, assuming we know the complete camera parameters of the x-ray fluoroscopy projective modality (Ganapathy 1984, Strat 1987, Rougée *et al* 1993, Hartley and Zisserman 2004). The camera parameters include $C(c_s, l_s, f, \Delta_u, \Delta_v, \delta_x, \delta_y, \delta_z, \theta, \phi, \psi)$. (c_s, l_s)

are the coordinates in the image where the beam is normal to the projection plane, f is the distance between the source and the projection plane, Δ_u and Δ_v are the pixel spacing in the (u, v)-axes, respectively on the projection plane, $\delta = (\delta_x, \delta_y, \delta_z)$ and (θ, ϕ, ψ) are the parameters defining the position and orientation of the camera in 3D space. The camera parameters are obtained from the DICOM header of the x-ray images. Using epipolar geometry, each of the 2D electrode positions obtained when forming our statistical model in θ_1 is backward projected to form a 3D line, $\mathbf{l}_b$, which is then forward projected to generate a 2D epipolar line, $\mathbf{l}_e$, in the current view, θ_2, that contains the corresponding electrode position. Hence, we generate 10 epipolar lines in θ_2 for each frame in the current view.

2.2.2. Blob detection and 2D CS catheter position estimation. We now determine the 2D position of the CS catheter in the new image in θ_2 and simultaneously determine its state of cardiorespiratory motion. Although the real-time catheter tracking algorithm (Ma *et al* 2010) is used in the training sequence, it fails in rotational datasets at view-angles that distort the solid circular shape of the CS catheter electrodes. Additionally, the multi-scale blob detection algorithm misdetects blobs at very low doses. Consequently, we cannot solely use this method for 2D catheter tracking in rotational sequences at low doses. Instead, we determine the cardiorespiratory state in the PCA model of θ_1 that produces epipolar lines that most closely match the catheter electrodes in the new image in θ_2. First, the fast multi-scale blob detector (Lindeberg 1993) is used to detect all possible electrode-like objects in the new image. The positions of all detected blobs are concatenated into a blob list, **BL**.

Using the PCA model, an instance of the CS catheter, $\hat{\mathbf{s}}$, can be generated in θ_1 according to

$$\hat{\mathbf{s}} = \bar{\mathbf{s}} + \sum_m w_m \mathbf{v_m} \tag{2}$$

where w_m are the weights for each eigenvector. If the first two eigenvectors are used then we can represent the instance by $\hat{\mathbf{s}}_{w_1 w_2}$. The weights $\hat{w}_1$ and $\hat{w}_2$ that represent the cardiorespiratory phase of the image for θ_2 are then estimated according to

$$\hat{w}_1, \hat{w}_2 = \underset{w_1 w_2}{\operatorname{argmin}}[D(\hat{\mathbf{s}}_{w_1 w_2}, \mathbf{BL}) + A(\hat{\mathbf{s}}_{w_1 w_2})] \tag{3}$$

where $D(\hat{\mathbf{s}}_{w_1 w_2}, \mathbf{BL})$ is a function that computes the sum of the minimum Euclidean distances between the epipolar lines generated by $\hat{\mathbf{s}}_{w_1 w_2}$ and their nearest corresponding blobs from **BL**. Its purpose is to position the epipolar lines so that they pass through the electrodes in the new view. $A(\hat{\mathbf{s}}_{w_1 w_2})$ is a function that computes the sum of angles between line segments joining successive blobs, in order for the optimisation to favour a smoothly curving line of blobs representing the electrodes. Motivated by the 2σ rule, which states that for a normal distribution, about 95% of the values lie within 2 standard deviations of the mean, our search space for the weights varies from $-2\sqrt{d_m}$ to $+2\sqrt{d_m}$, where d_m is the mth eigenvalue, and $1 \leqslant m \leqslant 2$. We minimized the function using a coarse-scale exhaustive search followed by an iterative optimisation using Matlab's lsqnonlin function with the trust-region-reflective algorithm (MATLAB Release 2013a, The MathWorks, Inc., Natick, Massachusetts, USA). For the application of our model on rotational sequences, where the CS catheter position deviation was larger, our search space for the weights varies from $-3\sqrt{d_m}$ to $+3\sqrt{d_m}$, to solve the optimisation. Additionally, for the phantom rotational datasets, the exact view angles for each frame were not available in the DICOM headers. Instead, initial estimates for the angles were computed by assuming a constant rotation speed. These were refined

by including a search over the angles ($\pm 5°$ from the initial estimate in steps of $1°$) in the exhaustive search for the PCA weights.

The resulting weights indicate the cardiorespiratory phases and the blobs from **BL** nearest to the epipolar lines give the catheter location in the new image.

2.3. Cardiac and respiratory gating of the current view

2.3.1. Cardiac gating. $\hat{w}_1$ is used to detect systolic frames, Ω_{sys}, of the image sequence. These are represented by the peaks of the variation of $\hat{w}_1$ with frame number, i.

$$\Omega_{\text{sys}} = \{i | w_{1,i-1} < w_{1,i} > w_{1,i+1}\} \tag{4}$$

2.3.2. Respiratory gating. The peaks of the variation of $\hat{w}_2$ over time represent end-inspiration (EI) respiratory frames, Ω_{EI}, while the troughs represent end-expiration (EX) respiratory frames, Ω_{EX}.

$$\Omega_{EI} = \{i | w_{2,i-1} < w_{2,i} > w_{2,i+1}\} \tag{5}$$

$$\Omega_{EX} = \{i | w_{2,i-1} > w_{2,i} < w_{2,i+1}\} \tag{6}$$

2.4. Correction of incorrectly annotated electrodes

In addition to generating gating information, the 2D electrode positions in the new view are determined as part of the gating process. These are useful in EP procedures, for example to register a 3D roadmap to the 2D x-ray images. However, it is possible that an electrode is associated with an incorrect blob in the new image, particularly in very-low-dose x-ray where there may be incorrect blobs close to the epipolar line, and these incorrect electrodes must then be corrected. The correction is an additional step in which the 3D position of the CS catheter is reconstructed from the 2D gated electrode positions in the two views.

Each set of CS electrode positions from the two projection planes is back-projected to reconstruct the CS catheter in 3D (Hawkes *et al* 1987, Penney 2001). The CS catheter's maximum inter-electrode distance is 5 mm and we consider incorrectly annotated electrodes as those that are located more than 9 mm away from their neighbouring electrodes. Clusters of more than 2 electrodes located less than 9 mm away from their neighbours are considered to be correctly annotated. A smooth spline, $\mathbf{s_r}$, $1 \leqslant r \leqslant R$, comprising a total of R points, is computed to fit the correctly annotated electrodes.

In cases where the proximal or the distal electrodes are incorrectly annotated, the two nearest spline points are used to extrapolate a 3D straight line, $\mathbf{l}_r$, passing through them. Taking all vectors as column vectors, the 3D point, $\mathbf{c}$, that minimizes the sum of squared errors to $\mathbf{l}_r$ and the back projection line $\mathbf{l}_b$ from the corresponding electrode in θ_1, is found using the 3D line-to-line distance equation:

$$\mathbf{c} = ((I - \mathbf{d} \cdot \mathbf{d}') + (I - \mathbf{d}_2 \cdot \mathbf{d}'_2))^{-1} \cdot [(I - \mathbf{d} \cdot \mathbf{d}') \cdot \mathbf{r} + (I - \mathbf{d}_2 \cdot \mathbf{d}'_2) \cdot \mathbf{r}_2] \tag{7}$$

I is the identity matrix, $\mathbf{d}$ is the unit direction vector of $\mathbf{l}_r$, $\mathbf{d}_2$ is the unit direction vector of $\mathbf{l}_b$, r is the nearest point on the spline, $\mathbf{r}_2$ is a point on $\mathbf{l}_b$ and $'$represents the transpose. We then correct our electrode to $\mathbf{r}_{\text{cor}}$, the point on line $\mathbf{l}_b$ that is closest to $\mathbf{c}$, and therefore $\mathbf{l}_r$, using (8)

$$\mathbf{r}_{\text{cor}} = \mathbf{r}_2 + ((\mathbf{c} - \mathbf{r}_2)' \cdot \mathbf{d}_2)\mathbf{d}_2 \tag{8}$$

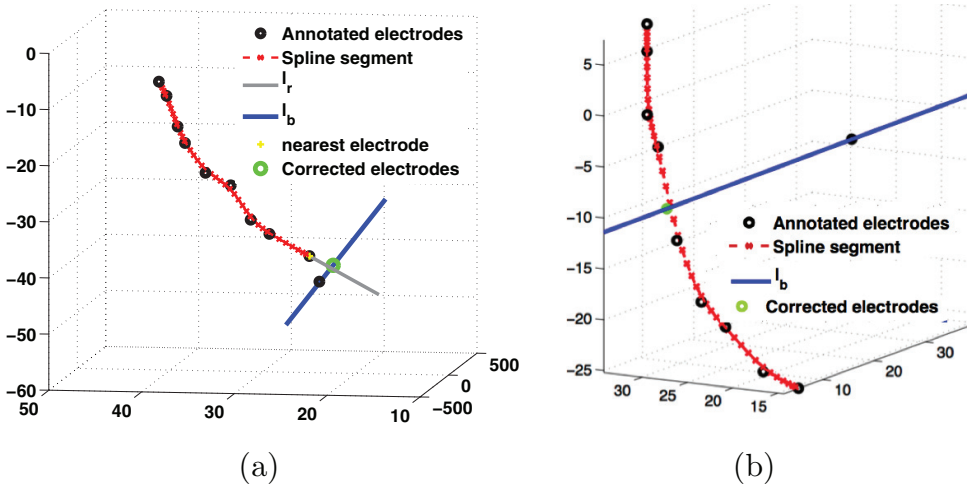

Figure 2. Graphical representation of correcting incorrectly annotated electrodes (a) at the end of the CS catheter and (b) in the middle of the CS catheter. The blue line is the backprojected line reconstructed from the corresponding uncorrected annotated electrode in the 1st view.

In cases where an incorrect electrode is found somewhere in the middle of the CS catheter, it is corrected to the point on line $\mathbf{l}_b$ that is closest to the nearest point on the spline segment, s_r, using (9)

$$\mathbf{r}_{\text{cor}} = \mathbf{r}_2 + ((s_r - \mathbf{r}_2)' \cdot \mathbf{d}_2)\mathbf{d}_2 \tag{9}$$

We then forward project our 10 final 3D electrode points to θ_2. Figures 2(a) and (b) illustrate the correction of annotated electrodes at the end and middle of the CS catheter, respectively.

3. Experiments

3.1. Application to gating and catheter tracking

3.1.1. Accuracy in multiplane sequence pairs at normal and low dose. The accuracy of our gating and catheter tracking were validated at both normal and low dose, on sequential biplane sequence pairs, from clinical and phantom data. The model was formed in one view at normal dose, and used to gate and track the catheter in a second view at either normal or low dose. A comparison to our existing single-view method (Panayiotou *et al* 2013) was performed to show the effect of the extra step of changing view angle. Comparison to all possible single view methods was not done, as this has already been done in our previous work (Panayiotou *et al* 2013) and was not our objective in this paper.

3.1.2. Accuracy of diastolic gating. Systole was chosen as opposed to diastole for validation of cardiac gating since the manual ground truth is more reliable for end-systole where rapid motion can be used as the visual cue. Although the majority of the experiments looked at only systole, one set of experiments was performed for diastolic accuracy in normal dose clinical images to ensure that the method is comparably accurate on diastolic frames.

3.1.3. Accuracy in rotational sequences at normal dose. Secondly, the accuracy of the technique was validated at normal dose on rotational angiography sequences, from clinical and

phantom data. The model was formed on a training view at a constant angle at normal dose, then applied to a rotational sequence with continuously changing angle between RAO90° and LAO90°.

3.1.4. View angle dependence. Finally, it is important to investigate the dependence of the phase determination accuracy on the view angle of the image sequence. Consequently, experiments were performed on phantom datasets with different view angles used for the formation of the statistical model in the training view. These were then applied to a rotational phantom dataset in the current view. This allowed comparison of different training angles and also investigation of how the accuracy varies with the current angle.

3.2. Methods of validation

3.2.1. Gold standard. To validate our technique, gold standard cardiorespiratory signals were generated along with a gold standard for the electrode positions in each x-ray image. The latter was done by the use of the CS tracking technique (Ma *et al* 2010). Manual tracking was performed in cases where the technique failed to accurately detect electrodes. This was done by manually localizing the centre of any misdetected electrode of the CS catheter. The 2D detection error of the CS tracking technique is 0.39 ± 0.22 mm over all electrodes (Ma *et al* 2010). The manual electrode detection gold standard was validated by two independent observers on 330 frames of phantom data (3300 electrode detections) and 122 frames of clinical data (1220 electrodes). The average Euclidean distance between the results of the two observers over all electrodes and frames of these randomly chosen phantom and rotational clinical sequences were 0.47 mm and 0.35 mm, respectively.

For the gating gold standard in clinical data, manual gating of the cardiac cycle at systole was performed by an experienced observer, by visually detecting the end of contraction of the left ventricle from the fluoroscopic left heart border shadow. Manual gating of the cardiac cycle at end-systole was further validated by three additional observers who were trained to identify the end-systolic frames throughout the x-ray sequences. All four chose identical systolic frames, indicating perfect precision of the gold standard.Manual gating of the cardiac cycle at end-diastole was also performed by three experienced observers, by visually detecting the end of relaxation of the left ventricle from the fluoroscopic left heart border shadow. No variation between the multiple observers was found. For the respiratory gating, a gold standard was obtained for the clinical data using either diaphragm or heart border tracking as described in Ma *et al* (2012). The respiratory signal obtained was cardiac gated using the manually identified systolic frames.

For the phantom sequences, two different clearly-visible regions of interest moving independently with cardiac and respiratory motion were automatically tracked using the diaphragm/heart border tracking method (Ma *et al* 2012). The gating accuracy of the automatic diaphragm/heart border tracking technique was found to be identical to manual gating based on landmarks attached to the phantom.

3.2.2. Gating accuracy measure. For both cardiac and respiratory gating, the absolute frame difference was computed between our technique and the gold standard techniques. Specifically, systolic, end-inspiration, end-expiration, and for one experiment end-diastolic, frames were recorded from our automatic and gold standard methods and their corresponding absolute frame differences were computed. Even though we do detect the whole cycle, for evaluation, we use only these peaks and troughs, where the gold standard is well-defined. Motion

gating accuracy objectives were set based on potential clinical applications that the proposed method could tackle. For motion gating of 3D rotational x-ray angiography sequences and 3D catheter reconstruction, cardiac motion is the limiting factor. These applications will use the diastolic cardiac phase, where the heart is more relaxed, and it is expected that its shape will be more repeatable over several cycles. Additionally, when registering a 3D model, the model is almost always from a diastolic image. Since the heart will be relatively stationary in the diastolic phase for a period of about 0.3 s, the motion gating accuracy objective is set to 0.1 s. Faultless gating results are signified when the absolute frame difference is within this motion gating accuracy objective.

3.2.3. 2D catheter tracking accuracy measure. 2D catheter tracking accuracy was evaluated simply as the distance between the measured electrode positions and gold standard positions. For cardiac catheterization procedures such as RF ablation, CS catheter tracking accuracy within 2 mm is an acceptable tolerance (Esteghamatian *et al* 2008).

3.3. Clinical protocol

All imaging was carried out using a monoplane 25 cm flat panel cardiac x-ray system (Philips Allura Xper FD10, Philips Healthcare, Best, The Netherlands) in one of the catheterization laboratories at St. Thomas' Hospital, London.

3.3.1. Intra-procedural image acquisition. Clinical images were acquired from 11 patients undergoing radiofrequency ablation procedures. Phantom images were acquired using a bespoke beating and breathing left ventricular phantom (Manzke *et al* 2010) with an inserted CS catheter, designed to emulate the clinical workflow of a typical catheterisation, as illustrated in figure 3(a). For this phantom, polyvinyl alcohol (PVA, Lenticats, GeniaLab, Braunschweig, Germany) (Mano *et al* 1986, Chu and Rutt 1997) was used as a tissue-mimicking material, to mimic the heart during cardiac interventions. A cylindrical PVA phantom with an inner radius of 6.6 cm, an outer radius of 8.2 cm and a length of about 9 cm, providing an initial wall thickness of about 1.6 cm, was generated using one freeze / thaw cycle at -35 °C/ $+20$ °C. The PVA phantom, illustrated in figure 3(b), was placed in an MR-compatible air-pressured actuator (Timinger *et al* 2004) which compresses and rotates the PVA according to a preset heart rate. Along with the cardiac motion, the phantom actuator can translate the phantom up and down to simulate breathing motion. For the experiments demonstrated in this chapter, the cardiac rate varied between 70 and 100 cycles per minute (cpm), while the respiratory rate varied between 8 and 12 cpm. X-ray imaging was performed at between 3 and 30 frames per second with an image size of either 512^2 or 1024^2 pixels in resolution, with a pixel size, $R_{\mathrm{x-ray}}$, of 0.25 mm pixel^{-1}. Included in this ratio is the typical magnification factor of the x-ray system.

3.3.2. Application of noise. The effect of low x-ray doses was investigated by adding Poisson noise to both the clinical and phantom test images. The magnitude of the noise varies across the image, as it depends on the local image intensity. The image noise is therefore specified in terms of the median value of the Poisson mean (Panayiotou *et al* 2013). We used SNR values of $\sqrt{50}$, $\sqrt{10}$, $\sqrt{8}$, $\sqrt{6}$ and $\sqrt{5}$, where the SNR value of $\sqrt{5}$ represents a dose reduction of more than 10 times. These values were chosen by initially applying our CS catheter tracking algorithm on low noise levels that are almost indistinguishable from the noise-free image, and then gradually increasing the noise level until the algorithm started to fail.

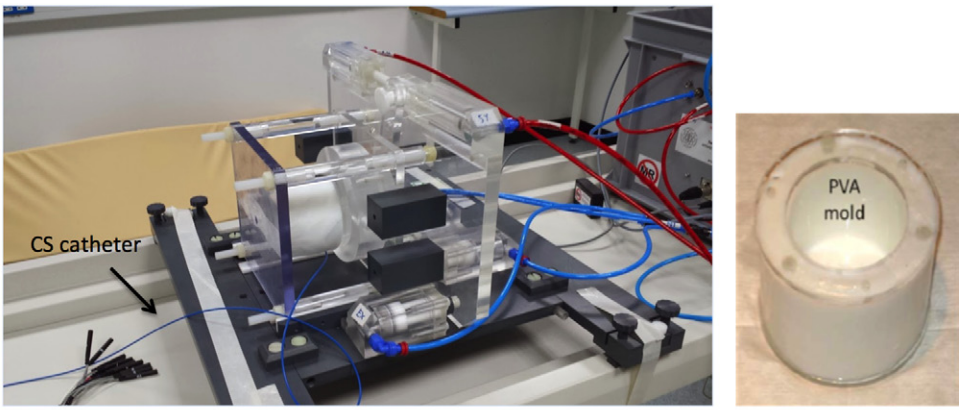

Figure 3. (a) Bespoke beating and breathing left ventricular phantom with an inserted CS catheter. (b) PVA cylinder mold.

3.3.3. Validation data. The multiplane normal and low-dose experiments used 3 sequential biplane clinical sequences (244 frames, 6 runs in total, running from a minimum of 8.0 to a maximum of 19.3 s, covering at least 2 respiratory cycles) and 2 sequential multiplane (one biplane and one triplane) phantom sequences (1741 frames, 5 runs in total, running from a minimum of 9.8 to a maximum of 22.7 s). The PCA model was formed for each sequence individually and the method run on each possible combination of sequence pairs, giving a total of 6 clinical and 8 phantom experiments.

For the rotation experiments, 3 clinical rotational x-ray angiography sequences (341 frames) and 2 phantom rotational x-ray sequences (540 frames) were used. Each sequence covered the range RAO 90° to LAO 90°. For the patient sequences the statistical model was formed on a monoplane x-ray sequence acquired for each patient in the AP view. For the application of our technique on the phantom rotational sequences, the model was formed on monoplane x-ray sequences in AP and RAO30° views in turn.

Finally, the angular dependency experiments used the same phantom rotational sequence. The training views used were PA, LAO 30° and RAO 30°.

4. Results

4.1. Application to multiplane sequence pairs at normal and low dose

4.1.1. Validation of CS catheter tracking. Figure 4 illustrates the results of the CS catheter tracking technique on the 1st image of an uncorrupted example x-ray sequence and the simulated low-dose images, with SNR values of $\sqrt{50}$, $\sqrt{10}$, $\sqrt{8}$, $\sqrt{6}$ and $\sqrt{5}$, respectively.

Figures 5(a) and 6(a) illustrate the CS catheter tracking median errors per electrode for phantom and patient x-ray images, respectively, at normal dose and for the 5 SNR values. Errors were calculated for each electrode and are shown in different grey scale colours, starting from the proximal (black colour) and moving to the distal (white colour) electrode. For the technique to be acceptable in clinical practice, failure cases were considered to be the ones where median errors per electrode were above 2 mm (Esteghamatian *et al* 2008). Figures 5(b) and 6(b) show the range of the values in terms of the first quartile (25th percentile) median

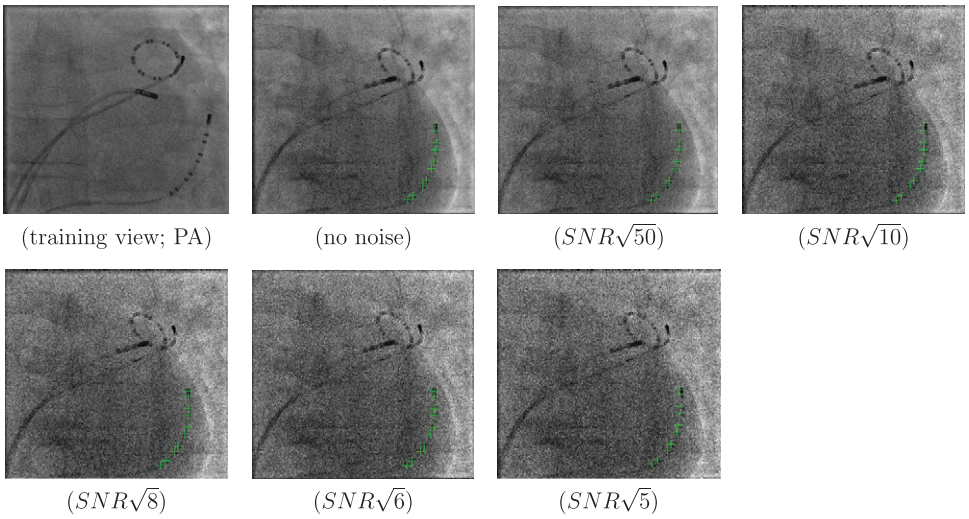

Figure 4. The PCA-view angle independent CS catheter tracking technique is illustrated in green crosses on an uncorrupted x-ray image during the ablation stage of a procedure to treat AF; and on the same x-ray image corrupted with different levels of Poisson noise. The first image illustrates the 1st frame of the training sequence used to build the statistical model.

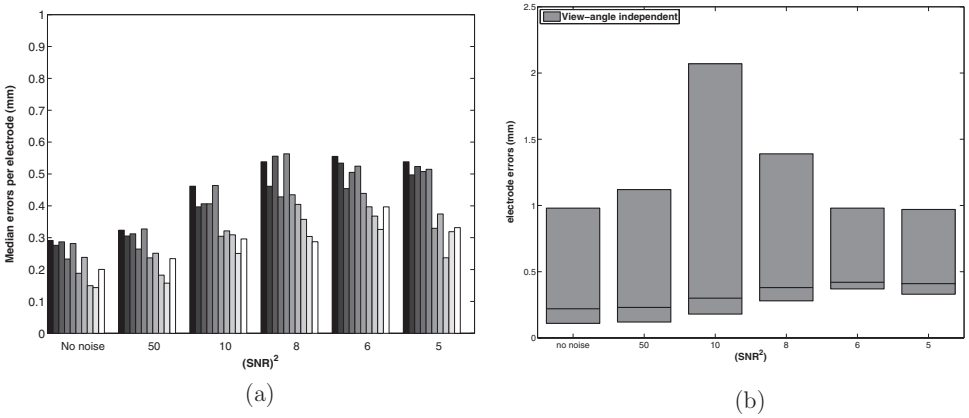

Figure 5. (a) Median errors per electrode with respect to the gold standard, for phantom x-ray sequences for the normal dose and five levels of SNR, where median errors are illustrated for all tracked CS electrodes. Different grey scale colour bars are used to distinguish the CS catheter electrodes, starting from the proximal (black colour) and moving to the distal electrode (white colour). (b) Illustration of the 25th percentile, median and 75th percentile values over all CS catheter electrodes in the data sets, for each noise level in the phantom data.

and third quartile (75th percentile) over all electrodes, for each noise level, for phantom and patient datasets, respectively. Success rates were also calculated and are shown as percentages (%) in figures 7(a) and (b), for the patient and phantom datasets.

4.1.2. Validation of cardiorespiratory motion gating. For cardiac gating validation, a plot of the first weight for the first 30 frames of an example clinical x-ray sequence is

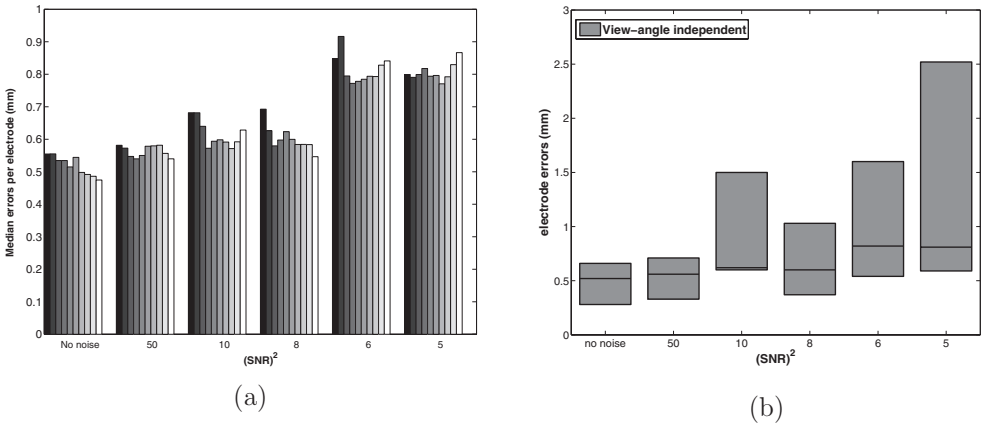

Figure 6. Catheter tracking errors. The meaning of the graphs is the same as in figure 5, but for clinical data.

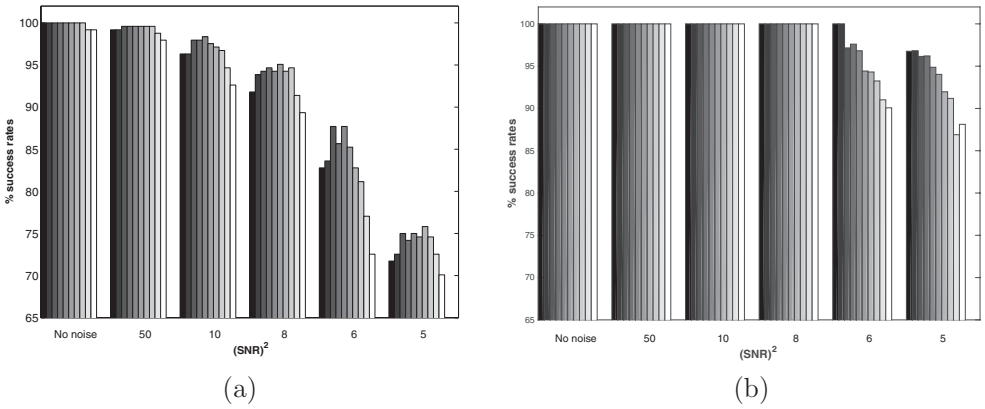

Figure 7. CS catheter tracking technique percentage success rates (%), for (a) clinical and (b) phantom x-ray sequences, respectively, for the normal dose and five different levels of SNR. Success cases are considered to be the ones where the median errors per electrode are below 2 mm.

illustrated in figure 8(a). The result of respiratory gating for the same sequence is shown in figure 8(b).

Figure 9 illustrates the frame difference errors in frequency distribution bar charts, i.e. the number of peaks or troughs with 0, 1 or 2 frames separation from the gold standard for the patient biplane sequences, for all gating tasks and noise levels. For both systolic and diastolic gating, the absolute frame difference was computed between the view-angle independent method and the gold standard methods on the normal dose images. The results showed no difference between end-systolic and end-diastolic gating so they are excluded from the figure. This indicates that the method is just as accurate on diastolic frames, and consequently the systolic accuracy results are relevant for applications that require diastolic gating. For a more comprehensive comparison, percentage (%) success rates for end-systolic, end-expiration (*EX*) and end-inspiration (*EI*) gating were also calculated and are shown in figure 10 for both the used phantom and clinical images. Using the model on unmodified clinical images for near-real time cardiorespiratory motion gating, end-systole,

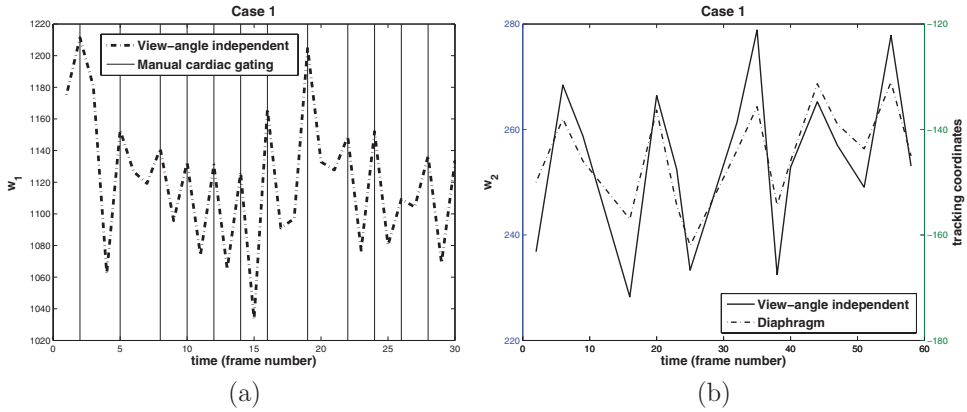

Figure 8. (a) Graphical representation of the variation of the first PC with x-ray frame number for an example dataset. The vertical black lines are the gold standard identification of end-systolic frames. (b) The respiratory traces obtained are illustrated for the same example case in a solid black line. The diaphragm tracking (gold standard) is also shown in a dashed-dot black line. The right *y*-axis scale corresponds to the gold standard trace while the left one corresponds to the trace obtained using the automatic technique.

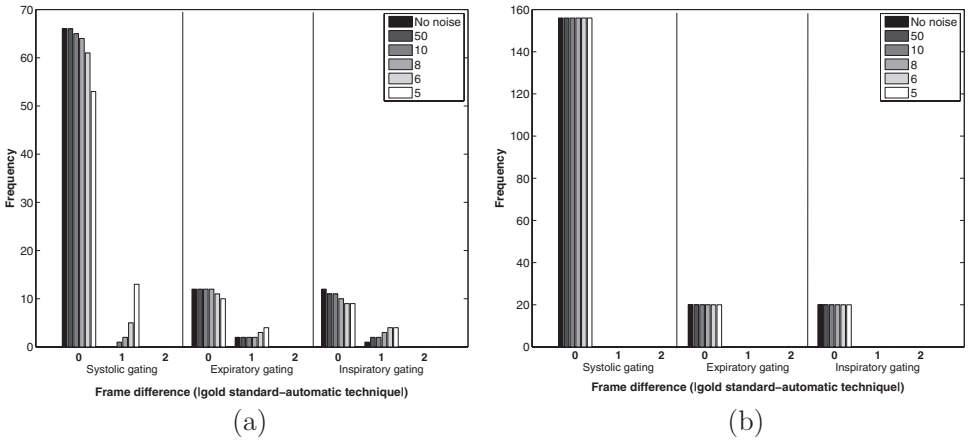

Figure 9. Distributions of frame difference errors for cardiac, *EX*, and *EI* gating for the uncorrupted and all noise corrupted x-ray sequences using the PCA-view-angle independent technique on (a) clinical and (b) phantom images.

EX and *EI* gating success rates of 100.0%, 85.7% and 92.3%, respectively, were established, based on the accuracy objective of 0.1 s. Additionally, gating success rates of 80.3%, 71.4% and 69.2% were established, even at the low SNR value of $\sqrt{5}$. Using the model on unmodified and modified phantom sequences, for near-real time cardiorespiratory motion gating, success rates of 100.0% were established for all gating tasks. To comparatively validate the technique to the Tracked-PCA method (Panayiotou *et al* 2013), where the statistical model was formed from normal dose images during a calibration phase and applied to low dose images acquired from the same view-angle, % success rates from both techniques for the same sequences are illustrated on the figure. No false positives or negatives (i.e. extra/fewer detected peaks/troughs) over the processed sequences were found. Outcomes show that the

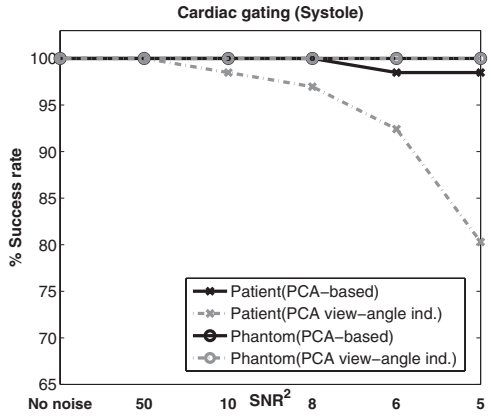

(a)

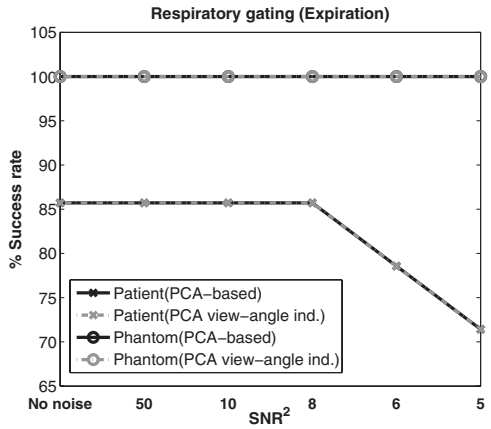

(b)

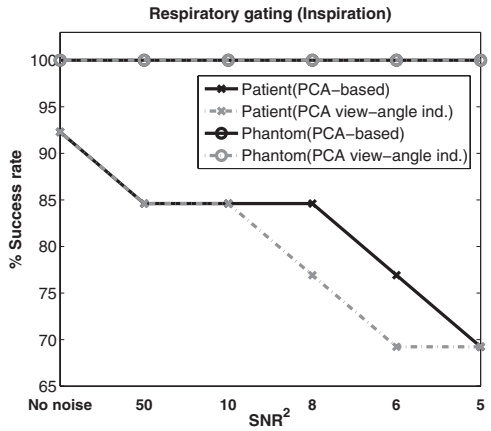

(c)

Figure 10. Percentage success rates for (a) cardiac, (b) *EX* and (c) *EI* gating for the uncorrupted and all noise corrupted x-ray sequences compared for the PCA view-angle independent and the previous Tracked-PCA technique on patient and phantom sequences.

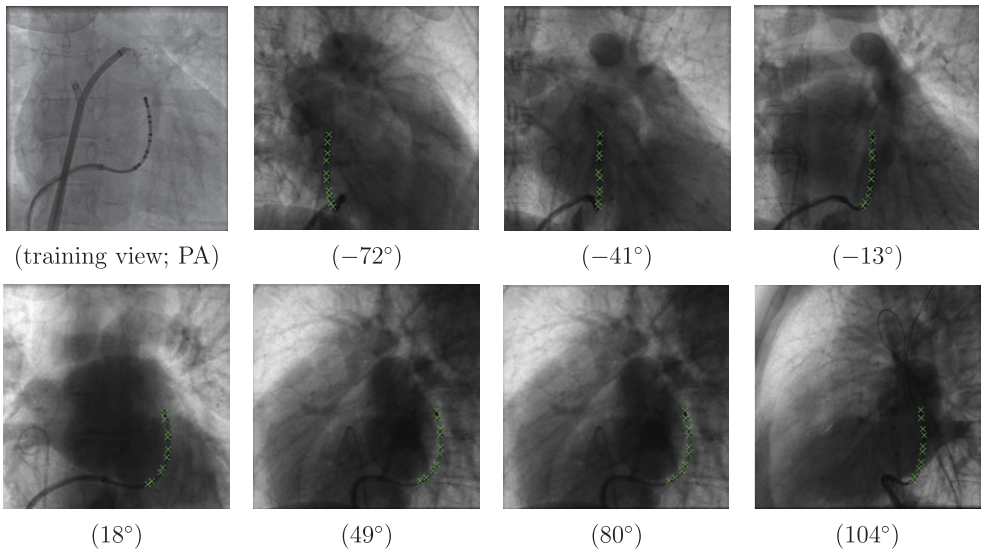

Figure 11. The view-angle independent CS catheter tracking technique is illustrated in green crosses on 3DRXA clinical images of evenly sampled view angles. The first image illustrates the 1st frame of the training sequence used to build the statistical model.

technique is robust and accurate in both CS catheter tracking and motion extraction even at the lowest SNR values of $\sqrt{5}$.

Regarding our algorithm's performance on the different experiments, depending on the step size of the optimisation, the execution time was between 0.41 and 1.73 s per frame running in Matlab on Windows 7 with a 3.4 GHz Intel Core i7 CPU and 8 GB of RAM.

4.2. Application to rotational sequences at normal dose

4.2.1. Validation of CS catheter tracking. Figures 11 and 12 illustrate the results of the CS catheter tracking technique on normal dose x-ray images at different view angles from a patient and a phantom example x-ray sequence, respectively. The results show that, this novel view-angle independent technique can successfully track the CS catheter in x-ray sequences where the angulation of the scanner is changed between frames. The multi-scale blob detection (Lindeberg 1993) and real-time tracking technique (Ma *et al* 2010) do not reliably detect the CS catheter electrodes in all views, even at normal dose, because of the different appearance of the electrodes at some angles.

Figure 13 illustrates (a) the CS catheter tracking technique median errors per frame per electrode and (b) the % success rates for the patient and phantom x-ray rotational sequences.

4.2.2. Validation of cardiorespiratory motion gating. For both cardiac and respiratory gating, the absolute frame difference was computed for the phantom procedures. For patient procedures the absolute frame difference was computed only for cardiac gating as patients were in breath-hold. The results can be seen in the frequency distribution bar charts in figure 14 for both patient and phantom rotational sequences. No false positives or negatives (i.e. extra/fewer detected peaks/troughs) over all processed sequences were found.

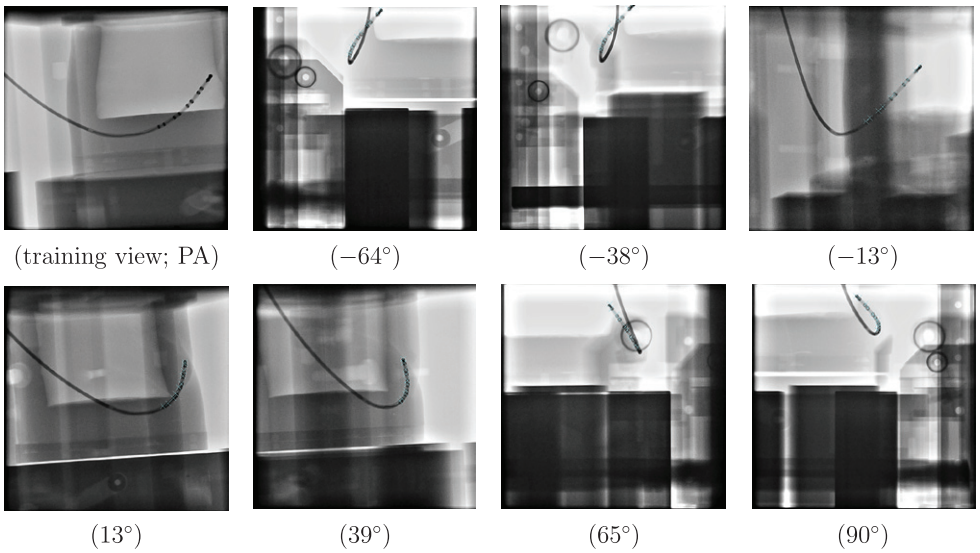

Figure 12. The view-angle independent CS catheter tracking technique is illustrated in cyan crosses on 3DRXA phantom images of evenly sampled view angles. The first image illustrates the 1st frame of the training sequence used to build the statistical model.

The results demonstrate that our proposed technique is robust and accurate in tracking the CS catheter and is doing a faultless job in extracting cardiorespiratory motion from any view-angle, over the range of 180°, in normal dose scenarios for rotational acquisitions.

4.2.3. Quantitative validation of view angle dependence. For both cardiac and respiratory gating, the gating success rate and the median errors per frame over all CS catheter electrodes were computed for the phantom experiments where the model was formed on different training views, PA, LAO 30° and RAO 30°, and tested on the same rotational sequence, ranging from RAO 90° to LAO 90°. This examines whether the difference in the viewing angles between the training and the current image sequences has an effect on the algorithm's success. The results for gating success rates were 100% in all cases. Therefore, the median errors of CS catheter tracking at each angle were compared and are shown in figure 15. CS catheter tracking is related to motion gating in the sense that a correctly annotated CS catheter would correspond to the best motion gating results we could obtain using our algorithm. CS tracking errors therefore indicate a potential for gating errors. The results show that there is no obvious dependence on the current or training angle. A paired two-sided Wilcoxon signed-rank test was conducted under the null hypothesis that there was no difference in building the model on different training views. The test was done on the median errors over all CS catheter electrodes with respect to viewing angles and was conducted for each of the viewing angle pairs. For all three pairs the p-values were more than 0.05, indicating that there is no statistically significant difference when building the model on different viewing-angles.

5. Discussion

In this manuscript, we have presented a novel technique for near-real time determination of cardiorespiratory gating using a PCA-based model of CS catheter motion that can be applied

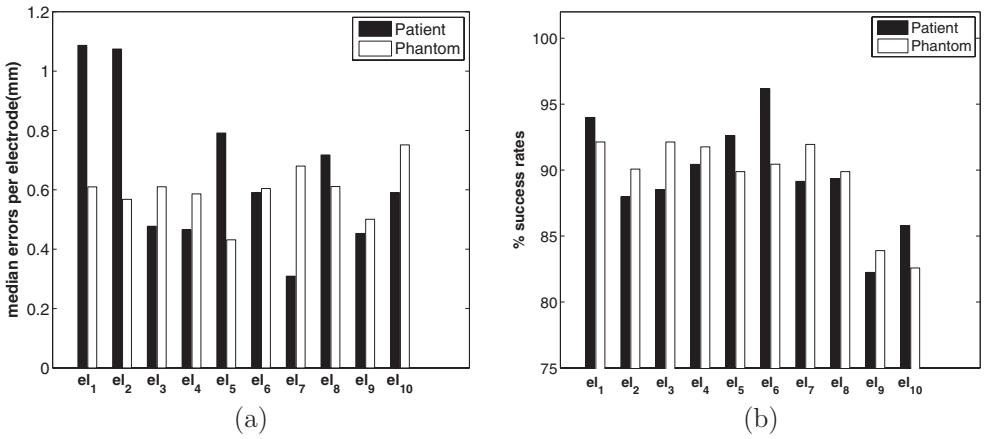

Figure 13. (a) Median errors per electrode with respect to the gold standard, for both patient and phantom x-ray rotational sequences. Median errors are illustrated for all tracked CS electrodes. (b) CS catheter tracking technique percentage success rates (%), for both patient and phantom x-ray rotational sequences.

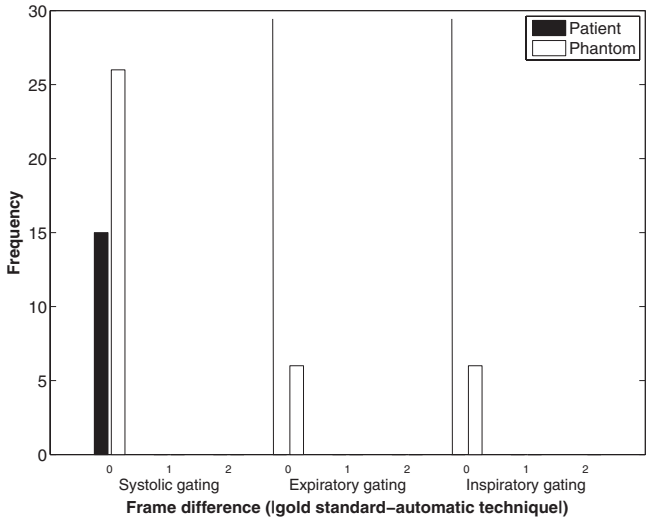

Figure 14. Frequency distributions of frame difference errors for cardiac gating on patient sequences and cardiac, end-inspiration and end-expiration gating on phantom sequences. In all cases, there are no gating errors.

to a secondary x-ray view. The technique is an extension of our previously proposed technique for automated image-based near-real time cardiorespiratory motion gating in normal and very low dose x-ray fluoroscopy images (Panayiotou *et al* 2013). It is developed to eliminate the requirement of our previous technique and all other model-based approaches to build a separate model for each x-ray view. Consequently, the current approach is x-ray system view-angle independent and therefore much more clinically useful.

To build our model in the training view the real-time tracking technique, proposed by Ma *et al* (2010), is used. This technique is robust and also performs very well in higher dose images. However, as illustrated in our previous work (Panayiotou *et al* 2013), success rates

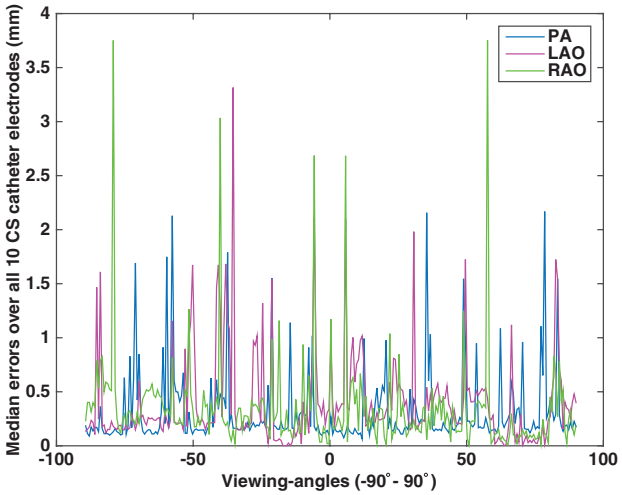

Figure 15. Median errors over all CS catheter electrodes with respect to viewing and training angles for phantom datasets.

calculated for our previously proposed catheter tracking technique are higher than those calculated for the real-time tracking technique in low dose x-ray sequences. In the clinical scenario, the real-time tracking technique will be used to form the PCA model from high dose x-ray images, where this technique is robust. Subsequently, the x-ray dose will be significantly reduced and our proposed view-angle independent technique will be employed for catheter detection in the current view, enabling the subsequent procedure to be carried out at very low x-ray dose.

One limitation of our technique is that if the CS catheter is advanced or pulled back before the second or subsequent views are acquired our statistical model would need to be rebuilt based on the new position of the CS catheter. However, one of the reasons that the CS catheter was chosen for our algorithm was because its position is commonly unchanged throughout the procedures.

In addition to gating, our technique is able to locate synchronised CS catheter electrode positions in the two views. However, even with accurate gating, correct annotation of catheter electrodes is not guaranteed. In very low dose applications there are cases where an electrode is incorrectly annotated, as a noise blob might be closer to the epipolar line than the actual catheter blob. As outlined in section 2.4 our algorithm is able to correct for this incorrect electrode annotation by first reconstructing the catheter in 3D from the two gated views. However, this electrode correction would fail if more than two incorrect neighbouring electrodes happen to be closer than 9 mm away from each other, as these would be seen as correct. We have not quantified the robustness experimentally, although a failure has never occurred in x-ray images with SNR values down to $\sqrt{5}$. Although correcting for these cases does not alter the gating accuracy, correct CS electrode annotation is clinically useful in EP procedures for relating signals measured at the electrodes to locations on the anatomy. Additionally, for rotational acquisitions, the electrodes can be removed by replacing with adjacent background prior to 3D reconstruction in an attempt to reduce motion artifacts. Our algorithm was able to detect the coronary sinus catheter with median errors of correctly-tracked electrodes not exceeding 1.2 mm, well below the acceptable value in clinical practice which is 2 mm (Esteghamatian *et al* 2008).

Moreover, regarding the algorithm's performance on the different experiments, depending on the step size, the execution time was between 0.41 and 1.73 seconds per frame. Hence, near-real time implementation is not currently achieved. However, code optimisation was not

the focus of this work and would need to be considered for real-time application. Additionally, a decrease in execution time will favour real-time motion compensation in the secondary view in sequences where x-ray imaging is performed at three frames per second or faster.

We have demonstrated the technique's use for gating of rotational sequences. Another potential clinical application of our technique is respiratory motion compensation of unseen images taken at any arbitrary projection, by driving the motion of the 3D MRI roadmaps fused onto live x-ray fluoroscopy. Existing motion compensation techniques (Giraud *et al* 2000, Jiang and Doppke 2001, Shechter *et al* 2005, King *et al* 2009a, Zhu *et al* 2010, Ma *et al* 2011, 2012) require a respiratory surrogate signal, such as diaphragm tracking, catheter motion or spirometry. This is used as an input to a motion model of the MRI roadmap, which can be a simple 1D translational correction, or a more complex motion model. The respiratory phase found using our technique could be used as the surrogate signal, with the benefit of requiring no additional equipment, working at low dose and at any view angle after an initial training step.

6. Conclusion

We have presented a novel and potentially clinically useful near-real time gating and catheter tracking technique for the determination of cardiorespiratory gating of x-ray fluoroscopic images in electrophysiology procedures. The technique is based on learning CS catheter motion using PCA and then applying the derived motion model to unseen images taken at arbitrary projections. Unlike most previously developed motion gating techniques, the main novelty of our technique is that it is x-ray system view-angle independent. Therefore, it is applicable and robust to cases where the angulation of the scanner is changed between frames. The method is fully automatic, requires no prior knowledge and can operate at around one second per image. Additionally, it is workflow-friendly, does not require any additional fiducial markers or contrast agent, and has the potential to greatly reduce radiation dose in image-guided cardiac catheter procedures. As a consequence radiation to patients and staff will decrease significantly. Future work will focus on implementing a new more accurate blob detection algorithm in an attempt to increase the % success rates of our technique. Additionally, we are planning to investigate the effect of a more explicit catheter detection, by including temporal constraints, i.e. the electrode will not move drastically between consecutive frames on the 2nd view. Finally, we intend to apply the method to the motion compensation task, using the respiratory gating trace to drive a suitable motion model.

Acknowledgments

The authors acknowledge financial support from the Department of Health via the National Institute for Health Research (NIHR) comprehensive Biomedical Research Centre award to Guy's and St Thomas' NHS Foundation Trust in partnership with King's College London and King's College Hospital NHS Foundation Trust. This work is funded by EPSRC programme grant EP/H046410/1. The authors would like to thank Philips Healthcare, Best, The Netherlands, for providing technical help with the prototype interventional guidance platform that was based on the commercial EP Navigator software.

References

Brost A, Liao R and Hornegger J 2010 Respiratory motion compensation by model-based catheter tracking during EP procedures *Med. Image Anal.* **14** 695–706

Brost A, Liao R, Strobel N and Hornegger J 2009 3-D respiratory motion compensation during EP procedures by image-based 3-D lasso catheter model generation and tracking *Medical Image Computing and Computer-Assisted Intervention–MICCAI* vol 5761 ed S B Heidelberg (Berlin: Springer) pp 394–401

Brost A, Wimmer A, Bourier F, Koch M, Liao R, Kurzidim K, Strobel N and Hornegger J 2012 Constrained registration for motion compensation in atrial fibrillation ablation procedures *IEEE Trans. Med. Imaging* **31** 870–81

Chu K and Rutt B 1997 Polyvinyl alcohol cryogel: an ideal phantom material for MR studies of arterial flow and elasticity *Magn. Reson. Med.* **37** 314–9

Condurache A, Aach T, Eck K, Bredno J and Stehle T 2005 Fast and robust diaphragm detection and tracking in cardiac x-ray projection images *Proc. SPIE Med. Imaging* **5747** 1766–75

De Buck S, Maes F, Ector J, Bogaert J, Dymarkowski S, Heidbuchel H and Suetens P 2005 An augmented reality system for patient-specific guidance of cardiac catheter ablation procedures *IEEE Trans. Med. Imaging* **24** 1512–24

Ector J, Buck S D, Huybrechts W, Nuyens D, Dymarkowski S, Bogaert J, Maes F and Heidbuechel H 2008 Biplane three-dimensional augmented fluoroscopy as single navigation tool for ablation of atrial fibrillation: accuracy and clinical value *Heart Rhythm* **5** 957–64

Esteghamatian M, Azimifar Z, Radau P and Wright G 2008 Real-time 2D-3D MR cardiac image registration during respiration using extended Kalman filter predictors *9th Int. Conf. on Signal Proc.* pp 1325–8

Ganapathy S 1984 Decomposition of transformation matrices for robot vision *Pattern Recognit. Lett.* **2** 401–12

Giraud P, Helfre S, Servois V, Dubray B, Beigelman-Grenier C, Zalcman-Liwartoski G, Straus-Zelter C, Neuenschwander S, Rosenwald J and Cosset J 2000 Evaluation of intrathoracic organs mobility using CT gated by a spirometer *Radiother. Oncol.* **56**

Gutiérrez L F *et al* 2007 Technology preview: x-ray fused with magnetic resonance during invasive cardiovascular procedures *Catheterization Cardiovascular Interventions* **70** 773–82

Hartley R and Zisserman A 2004 *Multiple View Geometry in Computer Vision* 2nd edn (Cambridge: Cambridge University Press)

Hawkes D, Colchester A and Mol C 1987 The accurate 3D reconstruction of the geometric configuration of vascular trees from x-ray recordings *Phys. Eng. Med. Imaging Springer Neth.* **119** 250–6

Jiang S and Doppke K 2001 Dosimetric effect of respiratory motion on the treatment of breast cancer with tangential fields *Med. Phys.* **28** 1228

Jolliffe I 2002 *Principal Component Analysis* (New York: Springer)

Khamene A, Warzelhan J, Vogt S, Elgort D, Chefd Hotel C, Duerk J, Lewin J, Wacker F and Sauer F 2004 Characterization of internal organ motion using skin marker positions *Medical Image Computing and Computer-Assisted Intervention—MICCAI* (*Lecture Notes in Computer Science* vol 3217) ed C Barillot *et al* (Berlin: Springer) pp 526–33

King A *et al* 2009a A subject-specific technique for respiratory motion correction in image-guided cardiac catheterisation procedures *Med. Image Anal.* **13** 419–31

King A, Rhode K, Razavi R and Schaeffter T 2009b An adaptive and predictive respiratory motion model for image-guided interventions: theory and first clinical application *IEEE Trans. Med. Imaging* **28** 2020–32

Kriatselis C, Nedios S, Akrivakis S, Tang M, Roser M, Gerds-Li J-H, Fleck E and Orlov M 2011 Intraprocedural imaging of left atrium and pulmonary veins: a comparison study between rotational angiography and cardiac computed tomography *Pacing Clin. Electrophys.* **34** 315–22

Lehmann G, Holdsworth D and Drangova M 2006 Angle-independent measure of motion for image-based gating in 3D coronary angiography *Med. Phys.* **33** 1311–20

Li J, Haim M, Movassaghi B, Mendel J, Chaudhry G, Haffajee C and Orlov M 2009 Segmentation and registration of three-dimensional rotational angiogram on live fluoroscopy to guide atrial fibrillation ablation: a new online imaging tool *Heart Rhythm* **231–7**

Lindeberg T 1993 Detecting salient blob-like image structures and their scales with a scale-space primal sketch: a method for focus-of-attention *Int. J. Comput. Vis.* **11** 283–318

Ma Y, King A, Gogin N, Gijsbers G, Rinaldi C, Gill J, Razavi R and Rhode K 2011 Comparing image-based respiratory motion correction methods for anatomical roadmap guided cardiac electrophysiology procedures *Functional Imaging and Modeling of the Heart* (*Lecture Notes in Computer Science* vol 6666) ed D Metaxas and L Axel (Berlin: Springer) pp 55–62

Ma Y, King A, Gogin N, Gijsbers G, Rinaldi C, Gill J, Razavi R and Rhode K 2012 Clinical evaluation of respiratory motion compensation for anatomical roadmap guided cardiac electrophysiology procedures *IEEE Trans. Biomed. Eng.* **59** 122–31

Ma Y, King A, Gogin N, Rinaldi C, Gill J, Razavi R and Rhode K 2010 Real-time respiratory motion correction for cardiac electrophysiology procedures using image-based coronary sinus catheter tracking *Medical Image Computing and Computer-Assisted Intervention–MICCAI* (*Lecture Notes in Computer Science* vol 6361) ed T Jiang *et al* (Berlin: Springer) pp 391–9

Ma Y *et al* 2009 Evaluation of a robotic arm for echocardiography to x-ray image registration during cardiac catheterization procedures *EMBC Annual Int. Conf. of the IEEE* pp 5829–32

Mageras G and Yorke E 2004 Deep inspiration breath hold and respiratory gating strategies for reducing organ motion in radiation treatment *Semin. Radiat. Oncol.* **14** 65–75

Mano I, Goshima H, Nambu M and Iio M 1986 New polyvinyl alcohol gel material for MRI phantoms *Magn. Reson. Med.* **3** 921–6

Manzke R, Lutz A, Schenderlein M, Bornstedt A, Chan R, Dietmeyer K and Rasche V 2010 A new PVA-based dynamic cardiac phantom for evaluation of functional MR imaging methods at 3 T *Proc. of the Int. Society for Magnetic Resonance in Medicine*

Paling M and Brookeman J 1986 Respiration artifacts in MR imaging: reduction by breath holding *J. Comput. Assist. Tomogr.* **10** 1080–2

Panayiotou M, King A, Bhatia K, Ma Y, Rinaldi C, Gill J, Cooklin M, O'Neill M, Housden R and Rhode K 2014 Extraction of cardiac and respiratory motion information from cardiac x-ray fluoroscopy images using hierarchical manifold learning *Statistical Atlases and Computational Models of the Heart. Imaging and Modelling Challenges* (*Lecture Notes in Computer Science* vol 8330) (Berlin: Springer) pp 126–34

Panayiotou M, King A, Housden R, Ma Y, Cooklin M, O'Neill M, Gill J, Rinaldi C and Rhode K 2014b A statistical method for retrospective cardiac and respiratory motion gating of interventional cardiac x-ray images *Med. Phys.* **41** 071901

Panayiotou M, King A, Ma Y, Rinaldi C, Gill J, Cooklin M, O'Neill M, Housden R and Rhode K 2013 A statistical model of catheter motion from interventional x-ray images: application to image-based gating *Phys. Med. Biol.* **58** 7543–62

Penney G P 2001 Registration of tomographic images to x-ray projections for use in image guided interventions *PhD Thesis* King's College London, University of London

Rhode K and Sermesant M 2011 Modeling and registration for electrophysiology procedures based on three-dimensional imaging *Curr. Cardiovascular Imaging Rep.* **4** 116–26

Rhode K *et al* 2005 A system for real-time XMR guided cardiovascular intervention *IEEE Trans. Med. Imaging* **24** 1428–40

Rougée A, Picard C, Ponchut C and Trousset Y 1993 Geometrical calibration of x-ray imaging chains for three-dimensional reconstruction *Comput. Med. Imaging Graph.* **17** 295–300

Schneider M, Sundar H, Liao R, Hornegger J and Xu C 2010 Model-based respiratory motion compensation for image-guided cardiac interventions *IEEE Conf. on Computer Vision and Pattern Recognition* pp 2948–54

Shechter G, Ozturk C and Resar J 2004 Respiratory motion of the heart from free breathing coronary angiograms *IEEE Trans. Med. Imaging* **23** 1046–56

Shechter G, Shechter B, Resar J and Beyar R 2005 Prospective motion correction of x-ray images for coronary interventions *IEEE Trans. Med. Imaging* **24** 441–50

Sra J, Narayan G, Krum D and Akhtar M 2006 Registration of 3D computed tomographic images with interventional systems implications for catheter ablation of atrial fibrillation *J. Interventional Cardiac Electrophysiology* **16** 141–8

Strat T 1987 Recovering the camera parameters from a transformation matrix *Readings Comput. Vis.* 93–100

Sundar H, Khamene A, Yatziv L, Wein W and Xu C 2009 Automatic image-based cardiac and respiratory cycle synchronization and gating of image sequences *Medical Image Computing and Computer-Assisted Intervention—MICCAI* (*Lecture Notes in Computer Science* vol 5762) ed G Yang *et al* (Berlin: Springer) pp 381–88

Timinger H, Krueger S, Borgert J and Grewer R 2004 Motion compensation for interventional navigation on 3d static roadmaps based on a dynamic motion model *Int. Congr. Ser.* **1268** 1055

Timinger H, Krueger S, Dietmayer K and Borgert J 2005 Motion compensated coronary interventional navigation by means of diaphragm tracking and elastic motion models *Phys. Med. Biol.* **50** 491

Truong M, Aslam A, Ginks M, Rinaldi C, Rezavi R, Penney G and Rhode K 2009 2D-3D registration of cardiac images using catheter constraints *Comput. Cardiology* pp 605–8

Zhu Y, Tsin Y, Sundar H and Sauer F 2010 Image-based respiratory motion compensation for fluoroscopic coronary roadmapping *Medical Image Computing and Computer-Assisted Intervention—MICCAI* (*Lecture Notes in Computer Science* vol 6363) ed T Jiang *et al* (Berlin: Springer) pp 287–294